

# Fracture analysis employing equivalent domain integral method and nodal integration techniques based on reproducing kernel particle method

Satoyuki Tanaka<sup>1</sup> · Akihiro Takata<sup>1</sup> · Ming-Jyun Dai<sup>1</sup> ·  
Hanlin Wang<sup>1</sup> · Shota Sadamoto<sup>1,2</sup>

Received: date / Accepted: date

**Abstract** A novel technique to evaluate fracture mechanics parameters is investigated employing the equivalent domain integral (EDI) method and nodal integration (NI) techniques. Galerkin-based meshfree method is adopted. Reproducing kernel (RK) is chosen for the meshfree interpolant. Stabilized conforming nodal integration (SCNI) and sub-domain stabilized conforming integration (SSCI) are adopted for numerically integrating the stiffness matrix. Voronoi diagram is employed to compute volume of each NI domain. The EDI method is addressed to evaluate the fracture mechanics parameters, i.e., energy release rate and stress intensity factors (SIFs). Because the displacement and its derivatives are computed based on SCNI/SSCI, the EDI can be discretized by summing up the physical quantities and volume of each cell/sub-cell. No special quadrature rule is required. To separate the energy release rate into the mixed-mode SIFs, interaction integral method is chosen. Efficient and accurate fracture parameter computation is achieved. Some numerical ex-

amples are demonstrated for mixed-mode fracture parameter evaluation and crack propagation analysis. Accuracy and effectiveness of the presented approach is studied.

**Keywords** Domain integral method · Nodal integration · Reproducing kernel · Fracture mechanics parameters

## 1 Introduction

Marine safety, as one of subjects with the most concern in maritime communities and industries, is under extensively investigation during past decades. Marine structures may encounter unexpected accidents, such as buckling, collision and grounding [1-5]. Moreover, corrosion and fatigue [6-11] can also be gradually accumulated during normal operation of the structures. Crack may occur occasionally and inevitably during these processes, and unstable crack propagation (CP) will lead to the damage of local and global structural integrity eventually. Therefore, fracture analysis is of vital significance in marine design and life prediction.

Stress intensity factor (SIF), introduced by Irwin [12], is usually recognized as one of the effective criteria in fracture mechanics. It is applied to represent the extent of stress concentration on the vicinity of crack tips. However, the geometrical singularity around crack tips will bring mathematical difficulties in the computation of stress and strain field straightforwardly. Therefore, a path independent method, named J-integral method, was introduced by Rice [13]. By appropriately selecting the integral contour, energy release rate can be calculated and the SIFs can also be determined.

Many efforts have been devoted to investigate SIFs employing several numerical methods. Chen [14] evalu-

---

S. Tanaka  
E-mail: satoyuki@hiroshima-u.ac.jp

A. Takata  
E-mail: m214588@hiroshima-u.ac.jp

M.-J. Dai  
E-mail: mingjyundai@gmail.com

H. Wang  
E-mail: hanlinwang@hiroshima-u.ac.jp

S. Sadamoto  
E-mail: sadamoto.shota@fujitsu.com

<sup>1</sup> Graduate School of Advanced Science and Engineering, Hiroshima University, Kagamiyama 1-4-1, Higashi-Hiroshima, 739-852, Japan

<sup>2</sup> Fujitsu Limited, 9-3, 4-1-1 Kamikodanaka, Nakahara-ku, Kawasaki city, Kanagawa 211-8588, Japan (Present address)

ated mode-I dynamic SIF of a two-dimensional (2D) central cracked strip by using Lagrangian finite difference method. Lin et al. [15] had constructed a hybrid crack element to finite element method (FEM) in the calculation of SIFs for bi-material interface cracks. Kishimoto et al. [16] modified the J-integral method to compute mixed-mode dynamic SIFs using FEM by considering the inertia effect. Li et al. [17] and Raju and Shivakumar [18] proposed an equivalent domain integral (EDI) form and its discretization technique for analyzing the  $J$  value and mixed-mode SIFs employing FEM. Yau and Wang [19] solved bi-material fracture problem by the interaction integral method (IIM). Belytschko and Black [20] proposed extended finite element method (X-FEM) and the fracture mechanics parameters are evaluated by IIM. Dolbow et al. [21] applied X-FEM in the research of mixed-mode SIFs on functionally graded materials. Nagashima et al. [22] had applied X-FEM to model the crack and evaluated the mode-I and -II SIFs on bi-material fractures. Tanaka et al. [23,24] analyzed several fracture problems by IIM based on X-FEM and wavelet Galerkin method [25]. These numerical methods have proved accuracy and reliability of the J-integral method and its discretization techniques in the SIFs evaluation on both homogeneous and non-homogeneous materials.

Meshfree and particle methods are an alternative methodologies to solve fracture problems. Based on local weighted least squares, Nayroles et al. [26] developed the diffuse element method (DEM). Comparing with FEM, DEM has stronger capability in solving PDEs and determining the derivatives of unknown functions. Belytschko et al. [27] further investigated the DEM and proposed the element free Galerkin method (EFGM). Based on EFGM, Pant et al. [28] evaluated mixed-mode SIFs by using IIM for bi-material interface problem. Pathak et al. [29] had further expanded researches on the bi-material interfacial cracks. Meanwhile, Jameel et al. [30] also employed EFGM in fatigue crack growth on different material discontinuous situations. Mohammadi Anaei et al. [31] analyzed fatigue crack growth of moderately thick plates using a meshfree method.

By considering properties of an window function, Liu et al. [32] had proposed the reproducing kernel particle method (RKPM), which is suitable for problems with large deformations and high gradients. It also has various applications in the analysis of elastic-plastic deformation, hyper-elasticity, and computational fluid dynamics [33]. Chen et al. [34,35] and Wang and Chen [36,37] proposed stabilized conforming nodal integration (SCNI) technique. Wang and Chen [38] developed sub-domain stabilized conforming integration (SSCI) technique. Recently, numerical integration methods in

the meshfree framework have been proposed in [39-47]. The SCNI and SSCI work well for the meshfree Galerkin formulation and its discretization technique to derive a smoothed displacement-strain relationship through Gauss divergence theorem. Silling et al. [48] also proposed a novel meshfree method, named peridynamics (PD). Based on state-based PD, Imachi et al. [49-51] solved the DSIFs on 2D plane by using the IIM. Moreover, fracture parameters were evaluated based on the EDI method and IIM [52,53] in PD framework. Overviews of meshfree methods could also be found in many literatures, such as [54,55].

Recently, Tanaka et al. [56] solved mixed-mode SIFs of 2D plane employing Galerkin-based RKPM meshfree method by the J-integral method [13]. The contour integral was discretized by SCNI and SSCI. Mixed-mode SIFs are extracted from the energy release rate by decomposing the displacement and stress fields into symmetric and antisymmetric components [57]. The fracture analysis method was applied to plate bending problems [58,59], folded structures [60] and curved shells [61].

In the present study, a discretization method to evaluate fracture mechanics parameters employing the EDI method and nodal integration (NI) techniques is newly proposed. SCNI and SSCI are employed and a Voronoi diagram is chosen to evaluate volume of each NI domain. Additionally, IIM is discretized by the NI techniques to handle mixed-mode fracture problems. Because the displacement, strain and stress components are computed on each cell/sub-cell by SCNI/SSCI, the EDI and IIM can be discretized by summing up the physical quantities and volume of the cells/sub-cells. No special quadrature rule is required. By employing this, stable and highly accurate results are obtained. As far as the authors' knowledge, there is no such kind of the NI discretization approach to the EDI method and IIM.

The outline of this paper can be shown as follow. In the second section, basic knowledge about Galerkin-based RKPM and NI techniques, i.e., SCNI and SSCI, will be presented for analyzing fracture mechanics problems. In the third section, the EDI discretization and mode splitting techniques with IIM by the NI methods will be discussed in detail. Then, in the fourth section, benchmark numerical examples for single and mixed-mode SIFs will be examined and validated. Additionally, application to CP simulation for a root crack in a welded joint is demonstrated. A brief summary will be provided in the final section.

## 2 Reproducing Kernel Particle Method

### 2.1 Governing equation

A boundary value problem (BVP) for a 2D cracked solid is considered. An elastic body including a crack and a hole is illustrated in Fig. 1(a). A global coordinate system  $(x_1, x_2)$  is defined.  $\mathbf{x} (= \{x_1, x_2\}^T)$  is a position vector and  $\mathbf{u} (= \{u_1, u_2\}^T)$  is a displacement vector. The analysis domain is  $\Omega$  and its boundary is  $\Gamma$ . The traction boundary is  $\Gamma_t$  and essential boundary is  $\Gamma_u$ .  $\bar{\mathbf{t}}$  is a traction vector and  $\bar{\mathbf{u}}$  is a prescribed displacement vector. The hole and crack is assumed as an external boundary. The upper/lower boundary of the crack are  $\Gamma_{c+}$  and  $\Gamma_{c-}$ , respectively.

Without the body force term, the BVP can be formulated, as:

$$\begin{aligned} \nabla \cdot \boldsymbol{\sigma} &= 0 & \text{in } \Omega, \\ \boldsymbol{\sigma}^T \cdot \mathbf{n} &= \bar{\mathbf{t}} & \text{on } \Gamma_t, \\ \boldsymbol{\sigma}^T \cdot \mathbf{n} &= 0 & \text{on } \Gamma_{c+}, \\ \boldsymbol{\sigma}^T \cdot \mathbf{n} &= 0 & \text{on } \Gamma_{c-}, \end{aligned} \quad (1)$$

where  $\nabla$  is a gradient operator,  $\boldsymbol{\sigma}$  is a Cauchy stress tensor.  $\mathbf{n}$  is a unit vector normal to  $\Gamma$ . On the crack segment  $\Gamma_{c+}$  and  $\Gamma_{c-}$ , a traction free condition is imposed. The displacement-strain relationship can be written, as:

$$\boldsymbol{\varepsilon} = \nabla_s \mathbf{u}. \quad (2)$$

$\nabla_s$  is the symmetric part of the gradient operator. The stress-strain relation is assigned with an elastic constant tensor  $\mathbf{C}$  considering plane strain/stress conditions, as:

$$\boldsymbol{\sigma} = \mathbf{C} : \boldsymbol{\varepsilon}. \quad (3)$$

Finally, the principle of virtual work is written, as:

$$\int_{\Omega} \boldsymbol{\varepsilon}(\delta \mathbf{u}) : \mathbf{C} : \boldsymbol{\varepsilon}(\mathbf{u}) d\Omega - \int_{\Gamma_t} \delta \mathbf{u} \cdot \bar{\mathbf{t}} d\Gamma_t = 0, \quad (4)$$

with  $\mathbf{u} = \bar{\mathbf{u}}$  on  $\Gamma_u$ .  $\delta \mathbf{u}$  and  $\boldsymbol{\varepsilon}(\delta \mathbf{u})$  are virtual displacement and virtual strain, respectively.

### 2.2 Reproducing kernel

The BVP is discretized by RKs. A schematic of the RK discretization method is shown in Fig. 1(b). The nodes are distributed in the body entirely. Volume of each node is evaluated by Voronoi diagram. RK is assigned for each node and it has a function support to interpolate physical values surrounding the node. The external boundaries including a hole edge as well as the crack segment of  $\Gamma_{c+}$  and  $\Gamma_{c-}$  are represented by set of the nodes.

The displacement vector  $\mathbf{u}(\mathbf{x})$  is interpolated, as:

$$\mathbf{u}(\mathbf{x}) = \sum_{I=1}^{np} \Psi_I(\mathbf{x}) \mathbf{u}_I. \quad (5)$$

$\Psi_I(\mathbf{x})$  and  $\mathbf{u}_I$  are RK and its coefficient vector for  $I$ -th node.  $np$  is total number of nodes in the analysis domain. The RK is written, as:

$$\Psi_I(\mathbf{x}) = \mathbf{H}^T(\mathbf{x}_I - \mathbf{x}) \mathbf{b}(\mathbf{x}) \phi_I(\mathbf{x}_I - \mathbf{x}), \quad (6)$$

where  $\mathbf{H}(\mathbf{x}_I - \mathbf{x})$  is a basis vector of the RK and  $\mathbf{b}(\mathbf{x})$  is the coefficient vector.  $\phi_I(\mathbf{x}_I - \mathbf{x})$  is an original kernel to generate the RK. A cubic B-spline function is adopted. Quadratic basis:  $\mathbf{H}(\mathbf{x}) = \{1 \ x_1 \ x_2 \ x_1^2 \ x_1 x_2 \ x_2^2\}$  is chosen as the basis vector. Derivation of  $\mathbf{b}(\mathbf{x})$  has included in previous literatures [34,36,62].

The standard RK in Eq. (6) does not possess so-called Kronecker delta property. When imposing the essential boundary conditions (BCs), singular kernel (SK) [63] is chosen. A one-dimensional (1D) arrangement of a SK and standard RKs is shown in Fig. 1(c). If SK is assigned to node  $I_{sk}$  to impose Kronecker delta property, standard RKs surrounding the node  $I_{sk}$  is modified. By choosing this, essential BC can be enforced accurately at the node position to the limit of machine precision.

Crack modeling is shown in Fig. 1(d). Double nodes are arranged along the crack segment. Visibility criterion and diffraction method [64,65] are utilized to represent displacement discontinuity of the crack. The visibility criterion is employed to cut the function support along the segment, and the diffraction method is utilized to represent crack tip position accurately by modifying the function support to wrap around the crack tip.

A sub-cell approach is chosen to accurately represent displacement discontinuity along the crack segment by dividing a Voronoi cell into a number of triangular domains. Moreover, an enriched basis vector [66,67] is employed to accurately represent near crack tip stress field, i.e.,  $\mathbf{H}(\mathbf{x}) = \{1 \ x_1 \ x_2 \ x_1^2 \ x_1 x_2 \ x_2^2 \ \sqrt{r'} \sin(\theta'/2)\}$ .  $(r', \theta')$  are a local polar coordinate system from the crack tip. The enriched basis vector is adopted if the crack tip is located within the function support of RKs. For further detail of the fracture mechanics analysis by RKPM, please see [56].

### 2.3 Nodal integration techniques

In a straightforward manner, the partial derivative of the displacement in Eq. (5) is evaluated in  $x_1$ - and  $x_2$ -

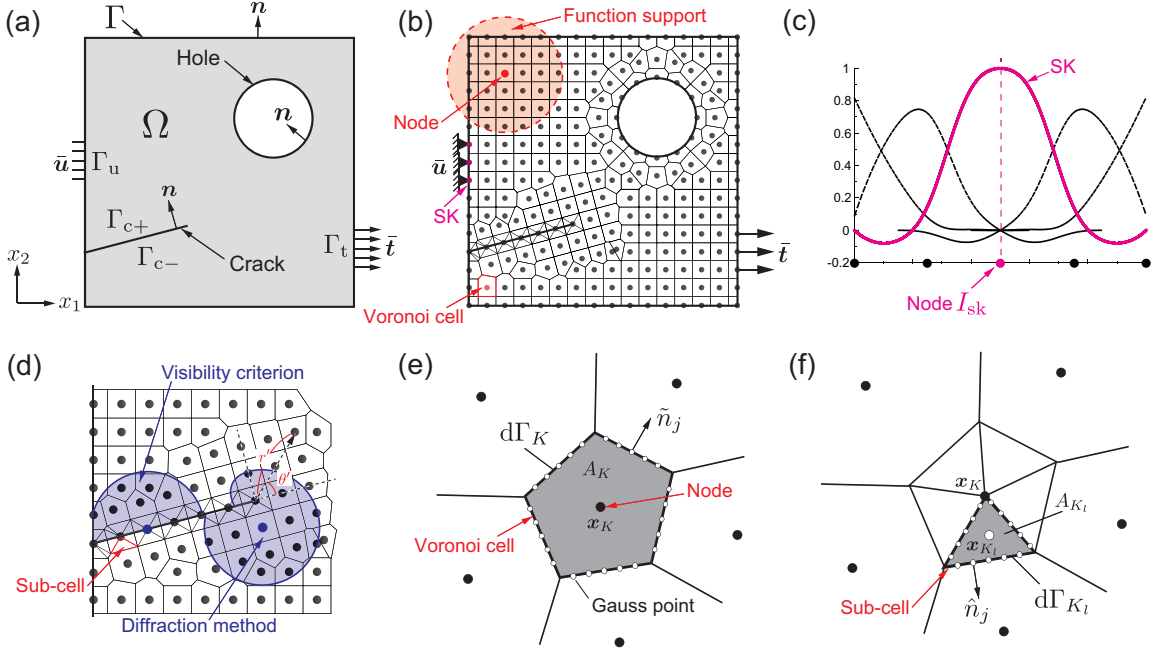


**Fig. 1** BVP and meshfree discretization technique for a 2D cracked elastic solid [(a) 2D BVP to be analyzed, (b) Meshfree discretization technique, (c) 1D arrangement of a SK and standard RKs, (d) Crack modeling, (e) SCNI, (f) SSCI].

directions, i.e.,

$$\boldsymbol{\varepsilon}(\mathbf{x}^G) = \sum_{I=1}^{np} \hat{\mathbf{B}}_I \mathbf{u}_I, \quad \hat{\mathbf{B}}_I = \begin{bmatrix} \Psi_{I,1} & 0 \\ 0 & \Psi_{I,2} \\ \Psi_{I,2} & \Psi_{I,1} \end{bmatrix}, \quad (7)$$

where  $\boldsymbol{\varepsilon}(\mathbf{x}^G) = \{\varepsilon_{11} \ \varepsilon_{22} \ 2\varepsilon_{12}\}^T$  is the strain vector at the evaluation point  $\mathbf{x}^G$ , e.g., a Gauss quadrature point.  $\hat{\mathbf{B}}_I$  is the displacement-strain matrix.  $\Psi_{I,i}$  ( $i=1,2$ ) is the partial derivative of the RKs for  $I$ -th node to  $i$ -th direction.

Voronoi diagram is adopted to define volume of each NI domain. Two kinds of NI techniques are employed. One is SCNI [34,35] and the other is SSCI [38]. SCNI to the  $K$ -th Voronoi cell is schematically illustrated in Fig. 1(e). For the SCNI, strain smoothing is carried out and the strain vector  $\tilde{\boldsymbol{\varepsilon}}(\mathbf{x}_K)$  is written, as:

$$\tilde{\boldsymbol{\varepsilon}}(\mathbf{x}_K) = \sum_{I=1}^{np} \tilde{\mathbf{B}}_I \mathbf{u}_I, \quad \tilde{\mathbf{B}}_I = \begin{bmatrix} \tilde{b}_{I1} & 0 \\ 0 & \tilde{b}_{I2} \\ \tilde{b}_{I2} & \tilde{b}_{I1} \end{bmatrix}, \quad (8)$$

where,

$$\tilde{b}_{Ij}(\mathbf{x}_K) = \frac{1}{A_K} \int_{\Gamma_K} \Psi_I \hat{n}_j d\Gamma_K. \quad (9)$$

$np$  is number of Voronoi cells.  $\mathbf{x}_K$  is a position vector of  $K$ -th node.  $A_K$  and  $\Gamma_K$  are area and edge of the  $K$ -th cell.  $\hat{n}_j$  is normal to the edge of the cell. A five point Gauss quadrature rule is employed for the line integration along  $\Gamma_K$ . In the SCNI technique, displacement

and strain/stress components are evaluated at  $\mathbf{x}_K$ . The physical values are smoothed for each cell.

While for SSCI, a Voronoi cell is divided by a number of triangular sub-cells as shown in Fig. 1(f). The strain vector  $\hat{\boldsymbol{\varepsilon}}$  is evaluated for each, as:

$$\hat{\boldsymbol{\varepsilon}}(\mathbf{x}_{K_l}) = \sum_{I=1}^{np} \sum_{l=1}^{ntri} \hat{\mathbf{B}}_I^l \mathbf{u}_I, \quad \hat{\mathbf{B}}_I^l = \begin{bmatrix} \hat{b}_{I1}^l & 0 \\ 0 & \hat{b}_{I2}^l \\ \hat{b}_{I2}^l & \hat{b}_{I1}^l \end{bmatrix}, \quad (10)$$

and where,

$$\hat{b}_{Ij}^l(\mathbf{x}_{K_l}) = \frac{1}{A_{K_l}} \int_{\Gamma_{K_l}} \Psi_I \hat{n}_j d\Gamma_{K_l}. \quad (11)$$

$ntri$  is number of the sub-cells in a Voronoi cell.  $\mathbf{x}_{K_l}$  is a position vector of a gravity center of  $l$ -th sub-cell.  $A_{K_l}$  is an volume of the sub-cell.  $\Gamma_{K_l}$  is a segment of the sub-cell and  $\hat{n}_j$  is normal to the segment. A five point Gauss quadrature rule is also employed to numerically integrate Eq. (11) as described in Fig. 1(f). In the SSCI technique, the displacement and strain/stress components are evaluated at  $\mathbf{x}_{K_l}$  and are smoothed in each sub-cell.

## 2.4 Discretization

By introducing the stress-strain relationship in Eq. (3) and the displacement-strain relationship in Eqs. (7), (8) and (10) into the principle of virtual work in Eq. (4), a

following linear simultaneous equation can be derived, as:

$$\mathbf{K}\mathbf{U} = \mathbf{f}, \quad (12)$$

where  $\mathbf{U}$  is an unknown vector in terms of the displacement vector  $\mathbf{u}$ .  $\mathbf{K}$  and  $\mathbf{f}$  are a global stiffness matrix and a traction vector, they are respectively written, as:

$$\mathbf{K} = \int_{\Omega} \mathbf{B}^T \mathbf{C} \mathbf{B} \, d\Omega, \quad \mathbf{f} = \int_{\Gamma_t} \boldsymbol{\Psi}^T \bar{\mathbf{t}} \, d\Gamma_t. \quad (13)$$

$\mathbf{B}$  is a displacement-strain relationship in terms of Eqs. (7), (8) and (10), respectively.  $\boldsymbol{\Psi}$  is a vector of the RKs. To numerically integrate the traction vector, a five point Gauss quadrature rule is employed along each edge of cell/sub-cells on  $\Gamma_t$ . After analyzing Eq. (12), the stress and strain components are evaluated based on the solution vector  $\mathbf{U}$  for each cell and sub-cells employing relation of Eqs. (7), (8) and (10).

### 3 Fracture Parameter Evaluation Methods

#### 3.1 J-integral and equivalent domain integral methods

Rice [13] proposed J-integral method to evaluate fracture mechanics parameters. The parameters can be evaluated by a contour integral surrounding the crack tip, and the method has a path independent property. Moreover, researchers [17] proposed an EDI method by transforming the contour integral to the area integral. This approach fit well with numerical discretization methods to analyze fracture mechanics parameters. Here, we briefly review the methodologies.

A schematic of the J-integral method for a 2D elastic solid is shown in Fig. 2(a). A straight crack is assumed and a local cartesian coordinate system  $(x'_1, x'_2)$  is defined from the crack tip. A contour  $s$  is taken by surrounding the crack tip from bottom to top crack surface.  $\mathbf{n}'$  ( $=\{n'_1, n'_2\}^T$ ) is a normal vector to the contour. Considering traction free condition on the crack faces, the  $J$  value is defined, as:

$$J = \int_s \left( W' n'_1 - \sigma'_{ij} \frac{\partial u'_i}{\partial x'_1} n'_j \right) ds. \quad (14)$$

$\sigma'_{ij}$  and  $u'_i$  are the stress and displacement components defined by the local coordinate system.  $ds$  is a segment of the contour.  $W'$  is a strain energy density, as:

$$W' = \int \sigma'_{ij} d\varepsilon'_{ij}. \quad (15)$$

where  $\varepsilon'_{ij}$  is the strain components in local coordinates.

The EDI method is schematically illustrated in Fig. 2(b). The two contours  $s_1$  and  $s_2$  are considered.  $s^+$

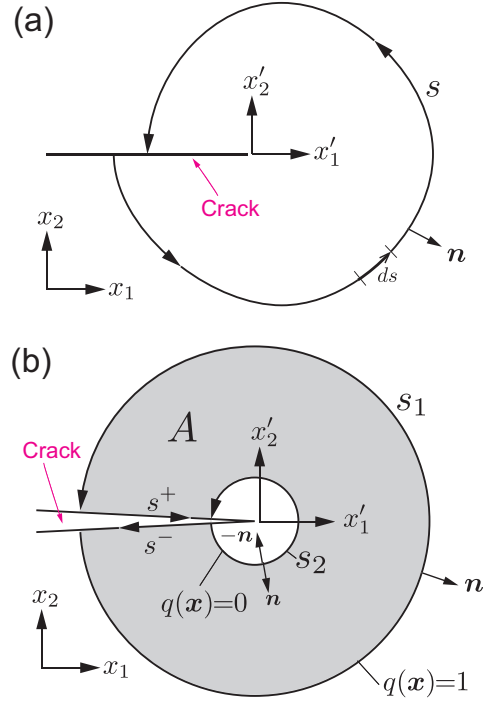


**Fig. 2** Schematic illustrations of the J-integral and EDI methods [(a) J-integral method, (b) EDI method].

and  $s^-$  are segments along top to bottom crack surfaces. Area  $A$  enclosed by a contour  $s_1 + s^+ - s_2 + s^-$  is considered. A smooth and continuous function  $q(\mathbf{x})$  is introduced that satisfy  $q(\mathbf{x})=0$  on  $s_1$  and  $q(\mathbf{x})=1$  on  $s_2$  within domain  $A$ . The contour integral in Eq. (14) can be rewritten through the divergence theorem, as:

$$J = \int_A \left( \sigma'_{ij} \frac{\partial u'_j}{\partial x'_1} - W' \delta_{1i} \right) \frac{\partial q(\mathbf{x})}{\partial x'_i} \, dA. \quad (16)$$

#### 3.2 Interaction integral method

To extract mixed-mode SIFs  $K_I$  and  $K_{II}$  from  $J$  value in Eq. (16), the IIM [19,20] is chosen. We consider two independent equilibrium states, i.e., an actual state (State  $\alpha$ )  $J^\alpha(u'_i{}^\alpha, \varepsilon'_{ij}{}^\alpha, \sigma'_{ij}{}^\alpha)$  and an auxiliary state (State  $\beta$ )  $J^\beta(u'_i{}^\beta, \varepsilon'_{ij}{}^\beta, \sigma'_{ij}{}^\beta)$ . A near crack tip asymptotic solution for linear fracture mechanics is chosen for the State  $\beta$ . The two states are superposed and the  $J$  value can be represented, as:

$$J^{\alpha+\beta} = J^\alpha + J^\beta + I^{\alpha+\beta}, \quad (17)$$

where  $J^\alpha$  and  $J^\beta$  are  $J$  values in terms of States  $\alpha$  and  $\beta$ .  $I^{\alpha+\beta}$  is an interaction term of the two states. The

term can be expressed by an integral form, as:

$$I^{\alpha+\beta} = \int_A \left( \sigma'_{ij}{}^{\alpha} \frac{\partial u_i^{\beta}}{\partial x'_1} + \sigma'_{ij}{}^{\beta} \frac{\partial u_i^{\alpha}}{\partial x'_1} - W'^{\alpha+\beta} \delta_{1j} \right) \frac{\partial q(\mathbf{x})}{\partial x'_j} dA. \quad (18)$$

$W'^{\alpha+\beta}$  ( $=\sigma'_{ij}{}^{\alpha} \varepsilon'_{ij}{}^{\beta} = \sigma'_{ij}{}^{\beta} \varepsilon'_{ij}{}^{\alpha}$ ) is the interaction strain energy density. Also, the term can be written, as:

$$I^{\alpha+\beta} = \frac{2}{E} (K_I^{\alpha} K_I^{\beta} + K_{II}^{\alpha} K_{II}^{\beta}), \quad (19)$$

where  $K_I^m$  and  $K_{II}^m$  ( $m=\alpha, \beta$ ) are the SIFs of the two states. In addition,  $\bar{E}=E$  for the plane stress condition and  $\bar{E}=E/(1-\nu^2)$  for the plane strain condition.  $E$  is Young's modulus and  $\nu$  is Poisson's ratio.

When the auxiliary state is chosen as mode-I ( $K_I^{\beta}=1, K_{II}^{\beta}=0$ ) or mode-II ( $K_I^{\beta}=0, K_{II}^{\beta}=1$ ), we obtain the mode-I or -II SIFs of the actual state, as:

$$K_I^{\alpha} = \frac{\bar{E}}{2} I^{\alpha+\beta}, \quad K_{II}^{\alpha} = \frac{\bar{E}}{2} I^{\alpha+\beta}. \quad (20)$$

### 3.3 Discretization technique for the equivalent domain integral method

The EDI method and IIM are discretized by the NI techniques. These operations can be carried out as a post process of the solution procedure. Schematics of the discretization method employing the NI techniques are shown in Fig. 3(a) and (b) for SCNI and SSCI, respectively. Equally spaced node distribution is arranged surrounding the crack tip and a rectangular domain is chosen for discretization of the EDI method.

When employing SCNI, the EDI can be discretized, as:

$$J = \sum_{K=1}^{np_A} \left( \sigma'_{ij}{}^{K} \frac{\partial u_j^{\prime K}}{\partial x'_1} - W'_K \delta_{1i} \right) \frac{\partial q(\mathbf{x})}{\partial x'_1} A_K, \quad (21)$$

where the physical values associated with the index "K" are evaluated at  $\mathbf{x}_K$ .  $np_A$  is number of Voronoi cells within domain  $A$ . While, when SSCI is employed, the EDI is expanded, as:

$$J = \sum_{K=1}^{np_A} \sum_{l=1}^{ntri} \left( \sigma'_{ij}{}^{K,l} \frac{\partial u_j^{\prime K,l}}{\partial x'_1} - W'_{K,l} \delta_{1i} \right) \frac{\partial q(\mathbf{x})}{\partial x'_1} A_{K_l}, \quad (22)$$

where the values associated with the indexes "K" and "l" are evaluated at  $l$ -th sub-cell of  $K$ -th node. It is noted that Voronoi cells across the crack segment as presented in Fig. 3(a). SSCI is employed for numerically integrate the stiffness matrix and the fracture parameter evaluations to introduce displacement discontinuity

across the crack.  $q(\mathbf{x})$  function is also schematically illustrated in Fig. 3(a) and (b). The function is linearly increasing/decreasing in the EDI domain along  $x'_1$ - and  $x'_2$ -directions.

The  $J$  value can be evaluated by superposing the physical values and volume of the cells/sub-cells as the post process. Very simple discretization can be achieved employing the Galerkin-based RKPM discretization and the NI techniques. No numerical integration table, e.g., Gauss quadrature rule, is required for the fracture parameter evaluation.

Generally, circular/rectangular EDI domain with regular mesh is adopted for accurate evaluation of the fracture mechanics parameters in FEM [17,18]. A general EDI domain with irregular tetrahedral mesh have been proposed [68,69]. However, researches on EDI with irregular mesh discretization are still few. Setting of the  $q(\mathbf{x})$  function will affect the accuracy of the fracture parameters. Careful examination is needed. Therefore, as the first attempt for the meshfree discretization, the EDI with regular node distribution is investigated.

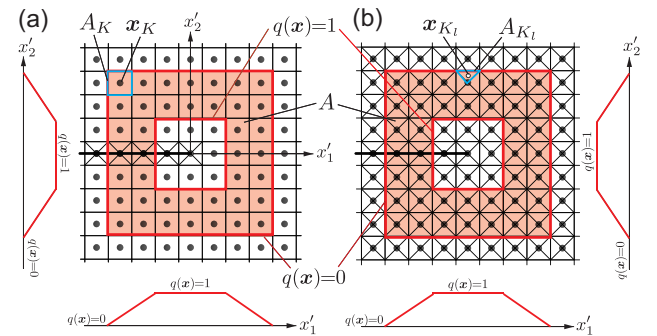


**Fig. 3** EDI discretization method by NI techniques [(a) SCNI, (b) SSCI].

### 3.4 Discretization technique of the interaction integral method

In the similar manner, IIM is discretized by adopting the NI techniques to the integral form of the IIM in Eq. (18). For SCNI case, it is discretized, as:

$$I^{\alpha+\beta} = \sum_{K=1}^{np_A} (F_K) \frac{\partial q(\mathbf{x})}{\partial x'_j} dA, \quad (23)$$

$$F_K = \sigma'_{ij}{}^{\alpha,K} \frac{\partial u_i^{\prime \beta,K}}{\partial x'_1} + \sigma'_{ij}{}^{\beta,K} \frac{\partial u_i^{\prime \alpha,K}}{\partial x'_1} - W_K'^{\alpha+\beta} \delta_{1j},$$

where  $u_i^{\prime m,K}$  and  $\sigma'_{ij}{}^{m,K}$  ( $m=\alpha, \beta$ ) are displacement and stress components.  $W_K'^{\alpha+\beta}$  is strain energy density

of the superimposed state. And, for SSCI case:

$$I^{\alpha+\beta} = \sum_{K=1}^{np_A} \sum_{l=1}^{ntri} (F_{K,l}) \frac{\partial q(\mathbf{x})}{\partial x'_j} dA,$$

$$F_{K,l} = \sigma'_{ij}{}^{\alpha,K,l} \frac{\partial u_i^{\beta,K,l}}{\partial x'_1} + \sigma'_{ij}{}^{\beta,K,l} \frac{\partial u_i^{\alpha,K,l}}{\partial x'_1} - W'_{K,l}{}^{\alpha+\beta} \delta_{1j}. \quad (24)$$

The physical values associated with “ $K$ ” and “ $l$ ” are evaluated in  $l$ -th sub-cell of  $K$ -th node as well as the EDI case in Eq. (22).

As for the  $q(\mathbf{x})$  in Eqs. (21)-(24), a plateau (square) type linear function is chosen as presented in Fig. 3(a) and (b).

#### 4 Numerical Examples

Four numerical examples are shown. To investigate accuracy in  $J$  value solved by the EDI discretization techniques for Eqs. (21) and (22), a cracked plate under mode-I problem is chosen as the first example. For the second example, a cracked plate under mixed-mode problem is analyzed to study accuracy in  $K_I$  and  $K_{II}$  evaluated by the IIM discretization technique for Eqs. (23) and (24). A path independency in the fracture mechanics parameters are also carefully examined. As the third example, a cantilever beam including a crack for various inclined angles are solved to demonstrate effectiveness of the present approach. As the final example, CP simulation for a root crack in a welded joint is carried out. All numerical results are compared with the reference solutions. The function support of the RKs set as 2.5 of a characteristic length between a node and its neighboring nodes.

Plane stress linear elastic analyses are carried out and the material parameters are  $E=206,000$  (MPa) and  $\nu=0.3$  for all numerical examples. Error between the computed results  $K_i$  and the reference results  $K_i^{\text{Ref}}$  are defined as:  $e_i = \{|K_i^{\text{Ref}} - K_i| / K_i^{\text{Ref}}\} \times 100\%$  ( $i=I, II$ ).

##### 4.1 Mode-I problem

A cracked rectangular plate is subjected to a tensile load as shown in Fig. 4(a). The width  $W$  and height  $H$  are 10 (mm), respectively. The crack length  $a$  is 5.0 (mm). Uniform tensile stress  $\sigma=1.0$  (MPa) is applied to top and bottom of the plate. This is pure mode-I case and the reference solution is  $K_I^{\text{Ref}}=11.93$  (MPa  $\text{mm}^{1/2}$ ) [70]. Accuracy in  $J$  value solved by the EDI discretization techniques are examined. The  $J$  value is transformed to the  $K_I$  value through  $J=K_I^2/E$ .

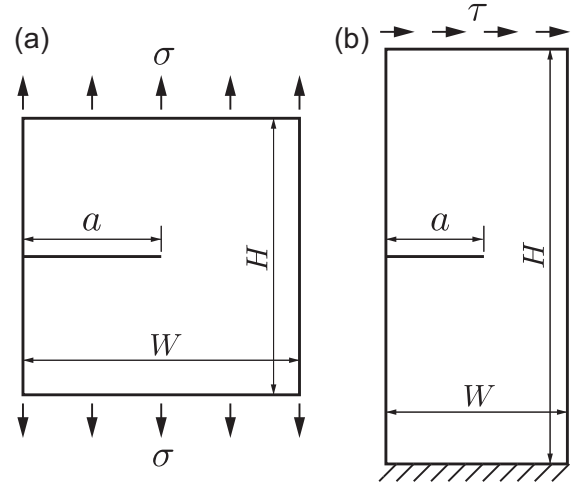


**Fig. 4** Cracked rectangular plates to be analyzed [(a) Mode-I case, (b) Mixed-mode case].

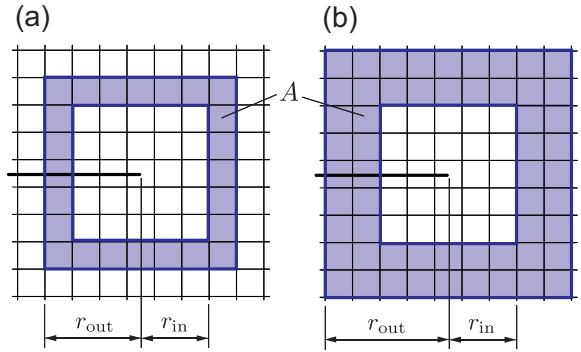


**Fig. 5** Definition of domain  $A$  for the EDI method and IIM [(a) Type-A, (b) Type-B].

The nodes are uniformly distributed to the cracked model in Fig. 4(a).  $21 \times 21$ ,  $41 \times 41$  and  $81 \times 81$  nodes models are arranged. Two kinds of EDI domains for the NI techniques, i.e., Type-A and Type-B are examined. It is schematically drawn in Fig. 5(a) and (b), respectively. Parameters  $r_{\text{in}}$  and  $r_{\text{out}}$  are introduced to define the EDI and IIM rectangular domain  $A$ . They are inside and outside radii of the domain from the crack tip. To check the path independent property, both parameters  $r_{\text{in}}$  and  $r_{\text{out}}$  are increased by keeping distance between  $r_{\text{out}}$  and  $r_{\text{in}}$ , i.e., one cell for Type-A and two cells for Type-B, respectively. For both cases,  $r_{\text{in}} \geq 1.5$  cell.

The computed  $K_I$  values are shown in Fig. 6(a) and (b). Fig. 6(a) is results by Type-A and SCNI case. The vertical axis is  $K_I$  values, and the horizontal axis is the distance parameter  $(r_{\text{in}} + r_{\text{out}})/2$  (mm). As number of nodes are increased, the results converge to the reference solution. However, a periodic oscillation can be seen in  $K_I$  even for the node density is increased. Also the path independency cannot be found. For the reference, the result evaluated by a contour integral (CI)

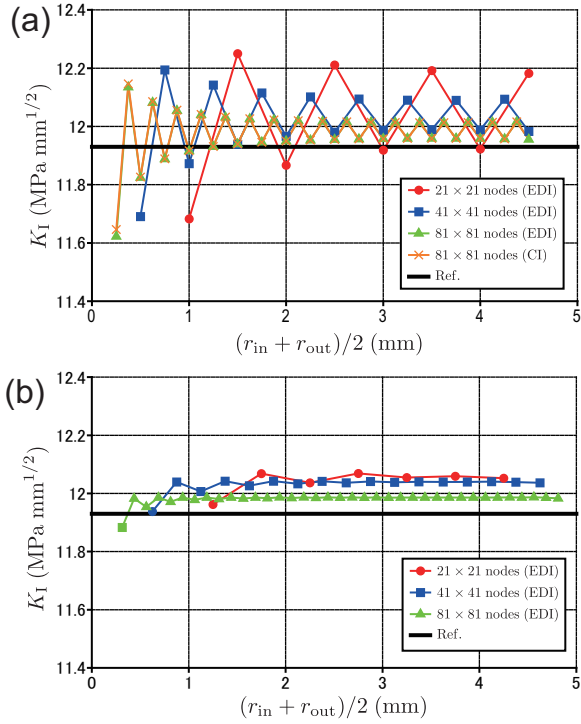


**Fig. 6**  $K_I$  for mode-I case evaluated by the EDI employing SCNI [(a) Type-A, (b) Type-B].

method with the NI integration techniques [56] is shown in Fig. 6(a) for  $81 \times 81$  nodes model. SCNI is employed for this calculation. Oscillation in the  $K_I$  values can be found and almost same results are obtained both the EDI and the contour integral discretization techniques.

For Type-B and SCNI case is examined. The results are shown in Fig. 6(b). The results converge the reference solution as number of nodes are increased. Surprisingly, a periodic oscillation cannot be seen and it has a path independency. When SCNI is employed, the physical values are smoothed within each cell. However, non-smooth values are sometimes obtained for the adjacent cells in analyzing steep gradients, e.g., stress concentration near the crack tip. Because only one cell is employed for width of the EDI domain for Type-A case, the oscillation occurs. While, by taking two cells for width of the EDI domain for Type-B case, the adjacent nodal values are averaged and the oscillation is canceled. Even more than two cells cases are studied, it is confirmed that  $J$  values evaluated by the EDI discretization technique satisfy the path independent property. Therefore, compared with the contour integral discretization technique by SCNI [56], effectiveness can be proved for the EDI case.

Additionally, SSCI is adopted for Type-A and Type-B cases. The results are shown in Fig. 7(a) and (b), respectively. For Type-A case, a small periodical oscillation can be seen but the amplitude is smaller than the

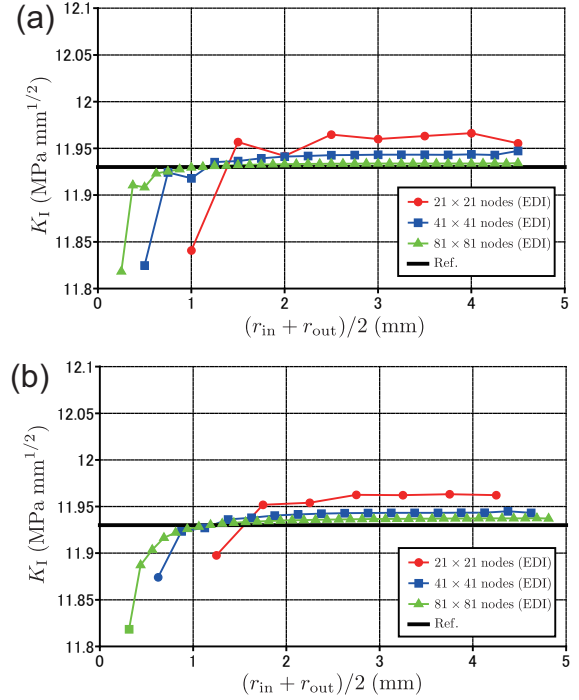


**Fig. 7**  $K_I$  for mode-I case evaluated by the EDI employing SSCI [(a) Type-A, (b) Type-B].

SCNI cases as depicted in Fig. 6(a) and (b). Moreover, the oscillation cannot be found even a coarse model is employed for Type-B case. For the SSCI case, the physical values are smoothed within each sub-cell and accuracy is improved further compared to the SCNI case. Results in  $K_I$  and their path independent properties are improved for both Type-A and Type-B cases.

The error  $e_I$  between the computed results and the reference solutions is studied. Type-B case is only examined and the results evaluated by SCNI and SSCI are shown in Table 1. The nodal spaces 0.5, 0.25 and 0.125 (mm) corresponding to  $21 \times 21$ ,  $41 \times 41$  and  $81 \times 81$  node models, respectively. The  $K_I$  values are evaluated for the EDI domain defined by  $(r_{in} + r_{out})/2$  from the crack tip.  $r_{in} = a/2$  is set for all cases. The error is decreased as finer models is employed. Results with SSCI cases are highly accurate than those of SCNI cases.

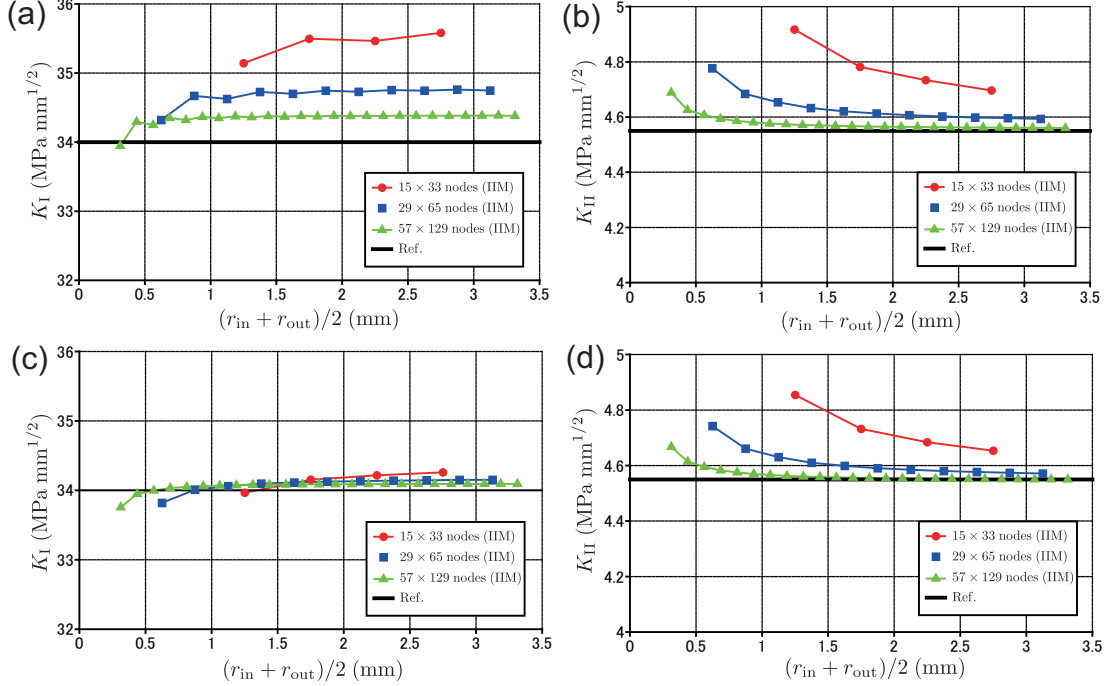
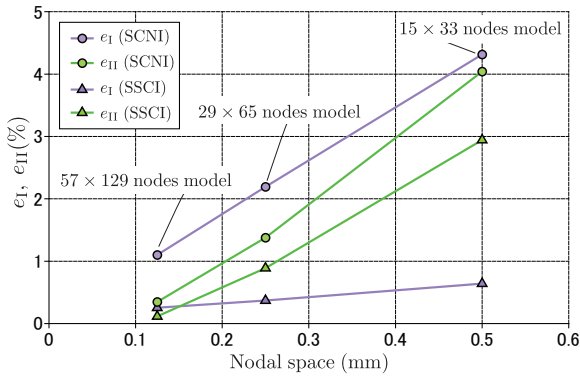
Through the investigation of the EDI discretization method by the NI techniques, it is confirmed that the approach is effective for the evaluation of  $J$  value. It is noted that Type-B and SSCI case is highly accurate and possess the path independent property for mode-I case.

## 4.2 Mixed-mode problem

To study accuracy in the proposed IIM discretization technique, a mixed-mode problem is analyzed. The anal-

**Table 1** Convergence studies of  $K_I$  for mode-I case (Type-B).

Type-B		SCNI		SSCI	
Nodal space	$(r_{in}+r_{out})/2$	$K_I$	$e_I$	$K_I$	$e_I$
(mm)	(mm)	(MPa mm <sup>1/2</sup> )	(%)	(MPa mm <sup>1/2</sup> )	(%)
0.5	2.75	12.069	1.166	11.962	0.272
0.25	2.625	12.037	0.894	11.943	0.108
0.125	2.5625	11.985	0.463	11.934	0.030

**Fig. 8** SIFs for mixed-mode case evaluated by the IIM for Type-B case [(a)  $K_I$  (SCNI), (b)  $K_{II}$  (SCNI), (c)  $K_I$  (SSCI), (d)  $K_{II}$  (SSCI)].**Fig. 9** Convergence of  $K_I$  and  $K_{II}$  for mixed-mode case (Type-B).

ysis model is shown in Fig. 4(b).  $W$  is 7.0 (mm) and  $H$  is 16.0 (mm).  $a$  is 3.5 (mm). The reference solutions are  $K_I^{Ref}=34.0$  and  $K_{II}^{Ref}=4.55$  (MPa mm<sup>1/2</sup>) [71].  $15 \times 33$ ,  $29 \times 65$  and  $57 \times 129$  uniformly distributed nodes models are employed. Type-B model is only employed based on the previous investigation.

$K_I$  and  $K_{II}$  results for SCNI cases are shown in Fig. 8(a) and (b), respectively. As well as the EDI discretization technique, a typical oscillation behavior in SIFs cannot be found and the results converge as the node density increases for both  $K_I$  and  $K_{II}$  cases. Additionally, the mixed-mode SIFs evaluated by SSCI is shown in Fig. 8(c) and (d), respectively. Reasonable results are obtained and the path independency can be found for both cases.

Convergence studies are carried out. The results are shown in Fig. 9. The vertical axis is error values  $e_i$  ( $i=I, II$ ) in the SIFs. The horizontal axis is the nodal spaces, i.e., 0.5, 0.25 and 0.125 (mm) correspond to  $15 \times 33$ ,  $29 \times 65$  and  $57 \times 129$  nodes models, respectively. The values are taken the distance parameter for the EDI domain  $(r_{in}+r_{out})/2$ . For all cases,  $r_{in}=a/2$  is chosen. As the node density increases, the results are monotonically converged. Convergence rate is better for the results with SSCI case than those with SCNI case.  $e_{II}$  for SSCI is much smaller than other three cases for coarse models, but it tends to be the same as other methods

for the finest model. For the mixed-mode problem, exact solution cannot be available. It is supposed that further refined reference solution is required for the precise examination. It is confirmed that the EDI and IIM discretization technique by the NI techniques are effective and highly accurate computations are carried out. The error values less than 1.0% in  $K_I$  and  $K_{II}$  are achieved for the nodal space 0.25 (mm) in Type-B and SSCI case.

#### 4.3 A cantilever beam including an inclined crack

To validate effectiveness of the present approach, a cantilever beam including a crack for various inclined angles are examined. The target problem is shown in Fig. 10(a).  $2a=3.75$  and 5.0 (mm) are respectively investigated for  $W=H=13$  (mm). The applied stress  $\sigma=1.0$  (MPa). The inclined angle  $\omega$  is varied from 0 to 180 (deg.). A meshfree model is presented in Fig. 10(b). Nodal distance of external region is 0.2 (mm) and internal region is 0.125 (mm). Total number of nodes are 8,842. A  $10 \times 10$  rectangular domain is arranged to surrounding crack tip for the evaluation of mixed-mode SIFs. SSCI and Type-B case is chosen. It is noted that no crack face contact treatment is introduced.

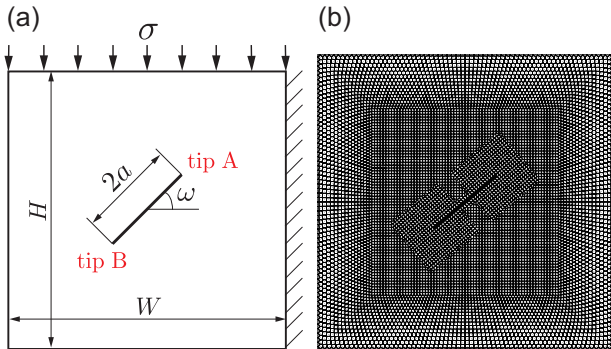


**Fig. 10** A cantilever beam including an inclined crack to be analyzed [(a) Analysis model and dimension of the target problem, (b) Meshfree model for  $2a=3.75$  (mm),  $\omega=40$  (deg.)].

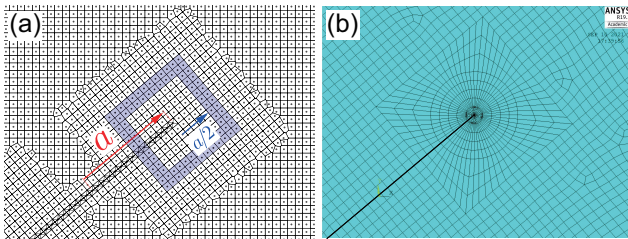


**Fig. 11** Modeling around the crack tip A for  $2a=3.75$  (mm),  $\omega=40$  (deg.) [(a) Meshfree model and the IIM domain, (b) FEM model].

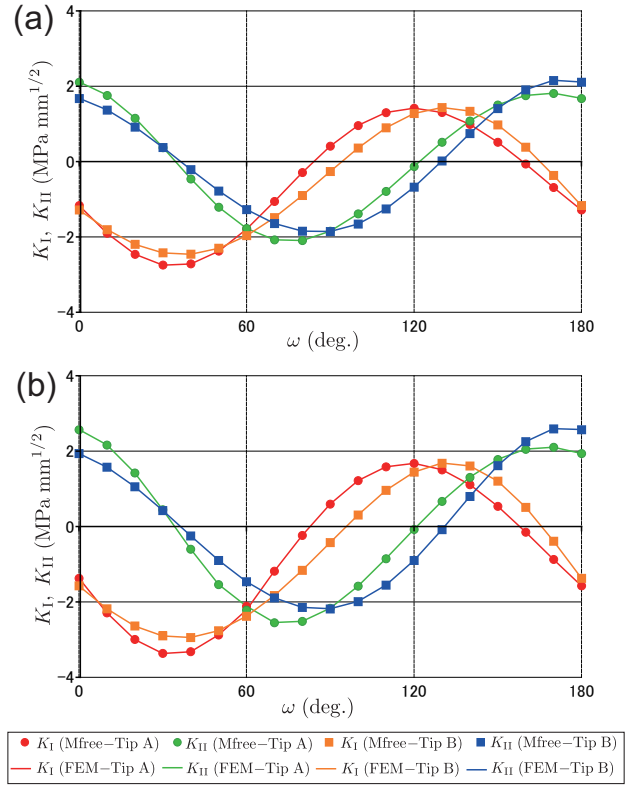


**Fig. 12** Mixed-mode SIFs for various crack angles  $\omega$  [(a)  $2a=3.75$  (mm), (b)  $2a=5.0$  (mm)].

A close-up view of the rectangular domain around crack tip A is shown in Fig. 11(a). A half crack length is  $a$ . For all computations,  $r_{in}=a/2$  is taken for all the cases, e.g., the blue colored region is the domain for the IIM discretization in the figure. For the reference solution, finite element (FE) computation is carried out. Fracture mechanics option of ANSYS\_APDL 19.2 [72] is applied. The FEs around the crack tip A is also shown in Fig. 11(b). Linear quadrilateral/triangular FEs are employed. The edges of the plate are uniformly discretized by 100 elements, and the skew mesh scheme is applied on the crack tips. PLANE183 is chosen. Around 0.0325 (mm) FEs are adopted near the crack tip. The smallest size of the element is 1/16 of that on the edges. Therefore, for different inclined angles, the total number of elements varies between 10,533 to 11,845. As for the evaluation of SIFs, the CINT command is employed directly. Total ten paths are taken. Except for the first path nearest the crack tip, the averaged values are employed as the reference solutions.

The results are shown in Fig. 12(a) and (b) for  $2a=3.75$  and 5.0 (mm), respectively. The meshfree results are good agreement with the reference solutions for both cases. Some of the  $K_I$  values take negative because the crack closure do not take into account. Additionally, numerical data of SIFs for  $2a=3.75$  and 5.0

**Table 2** Tip A and Tip B mixed-mode SIFs ( $\text{MPa}\sqrt{\text{mm}}$ ) for various crack angles  $\omega$  of  $2a=3.75$  (mm).

$\omega$ (deg.)	Tip A (Mfree)		Tip A (FEM)		Tip B (Mfree)		Tip B (FEM)	
	$K_I$	$K_{II}$	$K_I$	$K_{II}$	$K_I$	$K_{II}$	$K_I$	$K_{II}$
0	-1.166	2.108	-1.168	2.114	-1.283	1.677	-1.285	1.681
30	-2.745	0.372	-2.748	0.374	-2.420	0.374	-2.423	0.376
60	-1.791	-1.774	-1.793	-1.775	-1.965	-1.273	-1.967	-1.272
90	0.412	-1.845	0.412	-1.845	-0.260	-1.856	-0.261	-1.856
120	1.417	-0.128	1.418	-0.125	1.276	-0.676	1.277	-0.675
150	0.515	1.503	0.515	1.508	0.976	1.408	0.977	1.413

**Table 3** Tip A and Tip B mixed-mode SIFs ( $\text{MPa}\sqrt{\text{mm}}$ ) for various crack angles  $\omega$  of  $2a=5.0$  (mm).

$\omega$ (deg.)	Tip A (Mfree)		Tip A (FEM)		Tip B (Mfree)		Tip B (FEM)	
	$K_I$	$K_{II}$	$K_I$	$K_{II}$	$K_I$	$K_{II}$	$K_I$	$K_{II}$
0	-1.369	2.565	-1.371	2.573	-1.571	1.935	-1.574	1.940
30	-3.361	0.447	-3.366	0.449	-2.897	0.426	-2.902	0.429
60	-2.216	-2.112	-2.218	-2.115	-2.378	-1.462	-2.381	-1.461
90	0.596	-2.165	0.596	-2.165	-0.424	-2.182	-0.425	-2.182
120	1.675	-0.075	1.677	-0.071	1.446	-0.899	1.447	-0.899
150	0.538	1.778	0.538	1.783	1.204	1.616	1.205	1.621

(mm) are shown in Tables 2 and 3 for every 30 (deg.). The meshfree results are almost same with the reference solutions and the error in the SIFs are less than 1.0%. It is confirmed that the present approach is highly accurate and the path independent property is kept for fracture mechanics parameters.

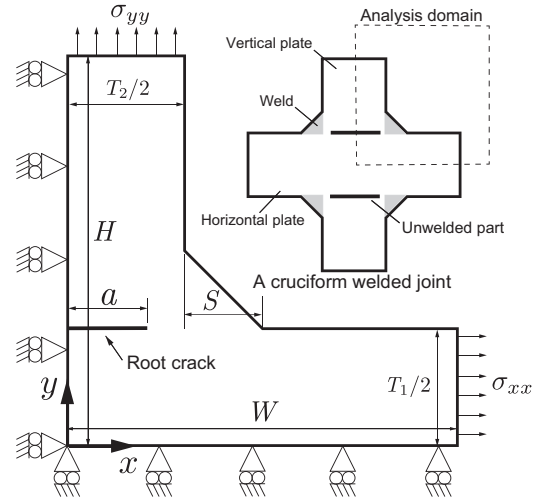
#### 4.4 CP simulation for a root crack in a welded joint

To further validate the present approach, a CP simulation is carried out. When constructing a steel cruciform welded joint, a fillet welding is adopted to join the vertical and horizontal plates. Unwelded part is remained in the connection. Fatigue crack sometimes generates from the unwelded part (root part). The fracture behaviors are important for the engineering application. The CP behaviors are studied based on the present approach.

The 2D welded joint model is shown in Fig. 13. A quarter model is taken assuming symmetric BCs. The plate thickness of the horizontal and vertical plates are  $T_1=T_2=15$  (mm), respectively. The length of the analysis domain is  $H=25$  (mm) and  $W=25$  (mm). The welded leg length is  $S=10$  (mm). A slit (a root crack) is introduced as the unwelded part, CP simulation is carried out. The slit has no gap to  $y$ -direction.

Based on Paris law CP simulation [73], the cyclic load is assumed to the welded joint for  $x$ - and  $y$ -direction. The stress amplitude is  $\bar{\sigma}_{xx}$  and  $\bar{\sigma}_{yy}$ , respectively. A stress ratio  $R=\bar{\sigma}_{xx}/\bar{\sigma}_{yy}$  is defined and three loading conditions  $R=-1, 0$  and  $1$  are investigated. The initial root crack length is  $a=5.0$  (mm).

CP simulation is carried out. The meshfree model is presented in Fig. 14. The whole view is Fig. 14(a).

**Fig. 13** A cruciform welded joint model and its BCs to be analyzed (Quarter model).

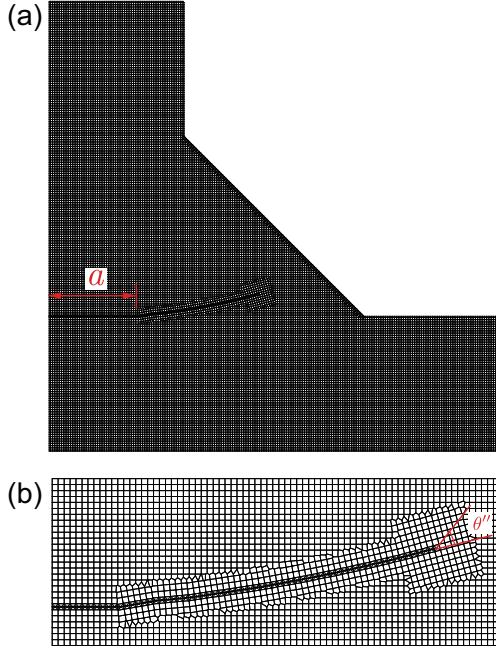
The joint is discretized by uniformly distributed nodes and Voronoi cells are placed for the NI. The average nodal distance is 0.125 (mm). SSCI is employed. IIM is adopted for the mixed-mode SIFs evaluation. The CP simulation is carried out until the crack penetrates the joint. The propagating crack is shown in Fig. 14(b). To predict crack propagation direction  $\theta''$ , Erdogan-Sih criterion [74] is adopted, as:

$$\theta'' = 2 \tan^{-1} \left[ \frac{1}{4} \left\{ \frac{K_I}{K_{II}} - \text{sign}(K_{II}) \sqrt{\left( \frac{K_I}{K_{II}} \right)^2 + 8} \right\} \right]. \quad (25)$$

After evaluating the direction, the crack is extended. The J-integral in Eq. (14) is formulated for a straight crack and the EDI domain should be defined for the straight crack region. In the CP simulation,  $5 \times 5$  nodes rectangular contours are adopted surrounding the crack

**Table 4** Mixed-mode SIFs for the initial crack  $a=5.0$  (mm) for different  $R$  values.

$R$	$K_I$ (MPa $\sqrt{\text{mm}}$ )			$K_{II}$ (MPa $\sqrt{\text{mm}}$ )		
	Mfree	MSC.Marc	Code_Aster	Mfree	MSC.Marc	Code_Aster
-1	334.1	334.8	334.9	-13.10	-13.30	-13.10
0	287.1	287.8	287.7	-25.00	-25.20	-25.20
1	240.0	240.7	240.7	-36.90	-37.20	-37.20

**Fig. 14** Meshfree model for the welded joint [(a) Whole view, (b) Close-up view around the crack].

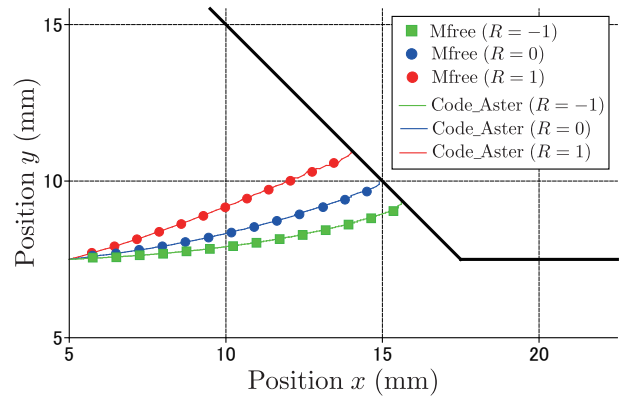
tip. A distance for six nodes is taken as the crack extension length for every step, i.e.,  $\Delta a=0.75$  (mm).

Mixed-mode SIFs for the initial crack is examined first. Different  $R$  at  $\bar{\sigma}_{yy}=100$  (MPa) is investigated. For the reference solutions, fracture mechanics option of MSC.Marc [75] and Code\_Aster [76-78] are employed. Very fine mesh and well converged results are adopted to evaluate the reference solutions. Linear quadrilateral FEs are employed in the MSC.Marc case. The element type is Element 3 (A four-node, isoparametric element). Whole structure is discretized by 0.1 (mm) mesh and 0.025 (mm) mesh chosen around the crack tip. The total number of nodes and elements are 42,903 and 42,169, respectively. LORENZI J-integral option is employed for the SIFs evaluation. While quadratic triangular FEs and X-FEM option are employed for Code\_Aster case. The element type is TR6. Whole structure is discretized 0.5 (mm) mesh and the mesh is refined at the crack tip. The mesh around the crack tip is about 0.0625 (mm). The total number of nodes and elements are 7,329 and 3,570, respectively. G-theta method is employed for the

SIFs evaluation [78].  $\Delta a=0.05$  (mm) for the CP simulation.

The SIFs results for the initial crack are shown in Table 4 for  $R=-1, 0$  and  $1$ , respectively. Type-B is chosen. The SIFs are evaluated with two domains, i.e.,  $r_{in}=2.5$  cell and  $r_{in}=3.5$  cell, respectively. And, the SIFs evaluated by the two domains are averaged. Among them, reasonable results are obtained for both  $K_I$  and  $K_{II}$ . When tensile stress is applied to  $y$ -direction ( $R=0$ ), the initial crack is under mixed-mode condition. Additionally, compressive stress is applied to  $x$ -direction, i.e.,  $R=-1$ ,  $K_I$  is increased and  $K_{II}$  is decreased compared with  $R=0$  case. While, tensile stress is added to  $x$ -direction ( $R=1$ ),  $K_I$  is decreased and  $K_{II}$  is increased.

The crack paths are shown in Fig. 15 for different  $R$  values. The results are compared with Code\_Aster X-FEM results. It is found that reasonable crack paths can be obtained for all cases. Based on Erdogan-Sih criterion, if ratio of  $|K_I/K_{II}|$  is smaller, the angle  $\theta''$  is larger. The inclination angle of the propagating crack to  $R=1/-1$  is larger/smaller compared to  $R=0$  case.

**Fig. 15** Crack paths for different  $R$  values employing the meshfree method and Code\_Aster X-FEM.

## 5 Conclusion

A novel fracture parameter evaluation technique is proposed. A Galerkin-based RKPM meshfree method is adopted. Highly accurate and stable solid mechanics analysis can be carried out by employing the meshfree

method not only intact but cracked problems. Continuous displacement and stress/strain fields can be obtained by the RK interpolants with quadratic basis. Accurate approximation is also carried out for steep gradients such as crack tip stress/strain fields by the enriched basis. Diffraction and visibility criterion are chosen to represent displacement discontinuity across the crack. The SCNI and SSCI are very suitable for numerically integrate the stiffness matrix of the intact/cracked problems.

The EDI method and IIM are discretized by the NI techniques. In the meshfree framework, the displacement, stress and strains can be evaluated by nodes. The physical values are averaged by each Voronoi cell and sub-cells. The EDI method and IIM are evaluated by the sum of the physical quantities and volume of the nodes. Mixed-mode fracture problems and CP simulation are analyzed. Through the careful examinations, it is confirmed that the proposed technique is effective and highly accurate.

## References

1. Calle MAG, Alves M (2015) A review-analysis on material failure modeling in ship collision. *Ocean Eng* 106:20-38
2. Liu B, Pedersen PT, Zhu L, Zhang S (2018) Review of experiments and calculation procedures for ship collision and grounding damage. *Mar Struct* 59:105-121
3. Cerik BC, Lee K, Park SJ, Choung J (2019) Simulation of ship collision and grounding damage using Hosford-Coulomb fracture model for shell elements. *Ocean Eng* 173:415-432
4. Tanaka S, Yanagihara D, Yasuoka A, Harada M, Okazawa S, Fujikubo M, Yao T (2014) Evaluation of ultimate strength of stiffened panels under longitudinal thrust. *Mar Struct* 36:21-50
5. Ozdemir M, Ergin A, Yanagihara D, Tanaka S, Yao T (2018) A new method to estimate ultimate strength of stiffened panels under longitudinal thrust based on analytical formulas. *Mar Struct* 59:510-535
6. Etube L (2001) *Fatigue and fracture mechanics of offshore structures*. Bury St Edmunds, UK
7. De Gracia L, Wang H, Mao W, Osawa N, Rychlik I, Storhaug G (2019) Comparison of two statistical wave models for fatigue and fracture analysis of ship structures. *Ocean Eng* 187:106161
8. Bhandari J, Khan F, Abbassi R, Garaniya V, Ojeda R (2015) Modelling of pitting corrosion in marine and offshore steel structures - A technical review. *J Loss Prev Process Ind* 37:39-62
9. Almarinaess A (1985) *Fatigue handbook: offshore steel structures*. United States
10. Corigliano P, Epasto G, Guglielmino E, Risitano G (2017) Fatigue analysis of marine welded joints by means of DIC and IR images during static and fatigue tests. *Eng Fract Mech* 183:26-38
11. Tanaka S, Maeda K, Takahashi H, Okada H, Yagi K, Osawa N (2021) A crack propagation simulation for a steel CHS T-joint employing an advanced shell-solid finite element modeling. *J Mar Sci Technol*, in press
12. Irwin GR (1957) Analysis of stresses and strains near the end of a crack traversing a plate. *ASME J Appl Mech* 24(3):361-364
13. Rice JR (1968) A path independent integral and the approximate analysis of strain concentration by notches and cracks. *ASME J Appl Mech* 35:379-386
14. Chen YM (1975) Numerical computation of dynamic stress intensity factors by a Lagrangian finite-difference method (the HEMP code). *Eng Fract Mech* 7(4):653-660
15. Lin KY, Mar JW (1976) Finite element analysis of stress intensity factors for cracks at a bi-material interface. *Int J Fract* 12(4):521-531
16. Kishimoto K, Aoki S, Sakata M (1980) Dynamic stress intensity factors using  $\dot{J}$ -integral and finite element method. *Eng Fract Mech* 13(2):387-394
17. Li FZ, Shih CF, Needleman A (1985) A comparison of methods for calculating energy release rates. *Eng Fract Mech* 21:405-421
18. Raju IS, Shivakumar KN (1990) An equivalent domain integral method in the two-dimensional analysis of mixed mode crack problems. *Eng Fract Mech* 37:707-725
19. Yau JF, Wang SS (1984) An analysis of interface cracks between dissimilar isotropic materials using conservation integrals in elasticity. *Eng Fract Mech* 20:423-432
20. Belytschko T, Black T (1999) Elastic crack growth in finite elements with minimal remeshing. *Int J Numer Methods Eng* 45:601-620
21. Dolbow JE, Gosz M (2002) On the computation of mixed-mode stress intensity factors in functionally graded materials. *Int J Solids Struct* 39(9):2557-2574
22. Nagashima T, Omoto Y, Tani S (2003) Stress intensity factor analysis of interface cracks using X-FEM. *Int J Numer Methods Eng* 56(8):1151-1173
23. Tanaka S, Okada H, Okazawa S, Fujikubo M (2013) Fracture mechanics analysis using the wavelet Galerkin method and extended finite element method. *Int J Numer Methods Eng* 93:1082-1108
24. Tanaka S, Suzuki H, Ueda S, Sannomaru S (2015) An extended wavelet Galerkin method with a high-order B-spline for 2D crack problems. *Acta Mech* 226:2159-2175
25. Tanaka S, Okada H, Okazawa S (2012) A wavelet Galerkin method employing B-spline bases for solid mechanics problems without the use of a fictitious domain. *Comput Mech* 50:35-48
26. Nayroles B, Touzot G, Villon P (1992) Generalizing the finite element method: diffuse approximation and diffuse elements. *Comput Mech* 10(5):307-318
27. Belytschko T, Lu YY, Gu L (1994) Element-free Galerkin methods. *Int J Numer Methods Eng* 37(2):229-256
28. Pant M, Singh IV, Mishra BK (2011) Evaluation of mixed mode stress intensity factors for interface cracks using EFGM. *Appl Math Model* 35(7):3443-3459
29. Pathak H, Singh A, Singh IV (2012) Numerical simulation of bi-material interfacial cracks using EFGM and XFEM. *Int J Mech Mater Des* 8(1):9-36
30. Jameel A, Harmain GA (2015) Fatigue crack growth in presence of material discontinuities by EFGM. *Int J Fatig* 81:105-116
31. Mohammadi Anaee MT, Khosravifard A, Bui TQ (2021) Analysis of fracture mechanics and fatigue crack growth in moderately thick plates using an efficient meshfree approach. *Theor Appl Fract Mech* 113:102943
32. Liu WK, Jun S, Zhang YF (1995) Reproducing kernel particle methods. *Int J Numer Methods Fluids* 20(8-9):1081-1106

33. Liu WK, Chen Y, Jun S, Chen JS, Belytschko T, Pan C, Uras RA, Chang CT (1996) Overview and applications of the reproducing Kernel Particle methods. *Arch Comput Methods Eng* 3(1):3-80
34. Chen JS, Wu CT, Yoon S, You Y (2001) A stabilized conforming nodal integration for Galerkin meshfree methods. *Int J Numer Meth Eng* 50:435-466
35. Chen JS, Yoon S, Wu CT (2002) Non-linear version of stabilized conforming nodal integration for Galerkin meshfree methods. *Int J Numer Meth Eng* 53:2587-2615
36. Wang D, Chen JS (2004) Locking-free stabilized conforming nodal integration for meshfree Mindlin-Reissner plate formulation. *Comput Meth Appl Mech Eng* 193:1065-1083
37. Wang D, Chen JS (2006) A locking-free meshfree curved beam formulation with the stabilized conforming nodal integration. *Comput Mech* 39:83-90
38. Wang D, Chen JS (2008) A Hermite reproducing kernel approximation for thin-plate analysis with sub-domain stabilized conforming integration. *Int J Numer Meth Eng* 74(3):368-390
39. Wang D, Wu J (2016) An efficient nesting sub-domain gradient smoothing integration algorithm with quadratic exactness for Galerkin meshfree methods. *Comput Methods Appl Mech Eng* 298:485-519
40. Wang D, Wu J (2019) An inherently consistent reproducing kernel gradient smoothing framework toward efficient Galerkin meshfree formulation with explicit quadrature. *Comput Methods Appl Mech Eng* 349:628-672
41. Wang J, Wu J, Wang D (2020) A quasi-consistent integration method for efficient meshfree analysis of Helmholtz problems with plane wave basis functions. *Eng Anal Bound Elem* 110:42-55
42. Wu J, Wang D (2021) An accuracy analysis of Galerkin meshfree methods accounting for numerical integration. *Comput Methods Appl Mech Eng* 375:113631
43. Huang TH, Wei H, Chen JS, Hillman M (2020) RKPM2D: An open-source implementation of nodally integrated reproducing kernel particle method for solving partial differential equations. *Comput Part Mech* 7:393-433
44. Hillman M, Chen JS (2016) An accelerated, convergent and stable nodal integration in Galerkin meshfree methods for linear and nonlinear mechanics. *Int J Numer Meth Eng* 107:603-630
45. Hillman M, Chen JS (2016) Nodally integrated implicit gradient reproducing kernel particle method for convection dominated problems. *Comput Methods Appl Mech Eng* 299:381-400
46. Hillman M, Chen JS, Chi SW (2014) Stabilized and variationally consistent nodal integration for meshfree modeling of impact problems. *Comput Part Mech* 1:245-256
47. Chen JS, Hillman M, Rüter M (2013) An arbitrary order variationally consistent integration method for Galerkin meshfree methods. *Int J Numer Meth Eng* 95:387-418
48. Silling SA, Epton M, Weckner O, Xu J, Askari E (2007) Peridynamic states and constitutive modeling. *J Elast* 88(2):151-184
49. Imachi M, Tanaka S, Bui TQ (2018) Mixed-mode dynamic stress intensity factors evaluation using ordinary state-based peridynamics. *Theor Appl Fract Mech* 93:97-104
50. Imachi M, Tanaka S, Bui TQ, Oterkus S, Oterkus E (2019) A computational approach based on ordinary state-based peridynamics with new transition bond for dynamic fracture analysis. *Eng Fract Mech* 206:359-374
51. Imachi M, Tanaka S, Ozdemir M, Bui TQ, Oterkus S, Oterkus E (2020) Dynamic crack arrest analysis by ordinary state-based peridynamics. *Int J Fract* 221:155-169
52. Dai MJ, Tanaka S, Bui TQ, Oterkus S, Oterkus E (2021) Fracture parameter analysis of flat shells under out-of-plane loading using ordinary state-based peridynamics. *Eng Fract Mech* 244:107560
53. Wang H, Tanaka S, Oterkus S, Oterkus E (2021) Evaluation of stress intensity factors under thermal effect employing domain integral method and ordinary state based peridynamic theory. *Continuum Mech Therm*, in press
54. Liu GR, Gu YT (2005) An introduction to meshfree methods and their programming. Springer, Dordrecht
55. Daxini SD, Prajapati JM (2014) A review on recent contribution of meshfree methods to structure and fracture mechanics applications. *The Sci World J* 2014:247172
56. Tanaka S, Suzuki H, Sadamoto S, Sannomaru S, Yu T, Bui TQ (2016) J-integral evaluation for 2D mixed-mode crack problems employing a meshfree stabilized conforming nodal integration method. *Comput Mech* 58(2):185-198
57. Ishikawa H (1980) A finite element analysis of stress intensity factors for combined tensile and shear loading by only a virtual crack extension. *Int J Fract* 16:R243-246
58. Tanaka S, Suzuki H, Sadamoto S, Imachi M, Bui TQ (2015) Analysis of cracked shear deformable plates by an effective meshfree plate formulation. *Eng Fract Mech* 144:142-157
59. Tanaka S, Suzuki H, Sadamoto S, Okazawa S, Yu TT, Bui TQ (2017) Accurate evaluation of mixed-mode intensity factors of cracked shear-deformable plates by an enriched meshfree Galerkin formulation. *Arch Appl Mech* 87(2):279-298
60. Tanaka S, Dai MJ, Sadamoto S, Yu TT, Bui TQ (2019) Stress resultant intensity factors evaluation of cracked folded structures by 6DOFs flat shell meshfree modeling. *Thin-Walled Struct* 144:106285
61. Dai MJ, Tanaka S, Sadamoto S, Yu T, Bui TQ (2020) Advanced reproducing kernel meshfree modeling of cracked curved shells for mixed-mode stress resultant intensity factors. *Eng Fract Mech* 233:107012
62. Sadamoto S, Tanaka S, Okazawa S (2013) Elastic large deflection analysis of plates subjected to uniaxial thrust using meshfree Mindlin-Reissner formulation. *Comput Mech* 52:1313-1330
63. Chen JS, Wang HP (2000) New boundary condition treatments in meshfree computation of contact problems. *Comput Methods Appl Mech Eng* 187:441-468
64. Organ D, Fleming M, Terry T, Belytschko T (1996) Continuous meshless approximations for nonconvex bodies by diffraction and transparency. *Comput Mech* 18:225-235
65. Krysl P, Belytschko T (1997) Element-free Galerkin method: Convergence of the continuous and discontinuous shape functions. *Comput Meth Appl Mech Eng* 148:257-277
66. Fleming M, Chu YA, Moran B, Belytschko T (1997) Enriched element-free Galerkin methods for crack tip fields. *Int J Numer Meth Eng* 40:1483-1504
67. Joyot P, Trunzler J, Chinesta F (2005) Enriched reproducing kernel approximation: Reproducing functions with discontinuous derivatives. In: Griebel M., Schweitzer M.A. (eds) *Meshfree Methods for Partial Differential Equations II. Lecture Notes in Comput Sci and Eng* 43:93-107 Springer, Berlin, Heidelberg
68. Okada H, Ohata S (2013) Three-dimensional J-integral evaluation for cracks with arbitrary curvatures and kinks based on domain integral method for quadratic tetrahedral finite element. *Eng Fract Mech* 109:58-77
69. Daimon R, Okada H (2014) Mixed-mode stress intensity factor evaluation by interaction integral method for quadratic tetrahedral finite element with correction terms. *Eng Fract Mech* 115:22-42

70. Bowie OL (1972) Solutions of plane crack problems by mapping technique (Chapter 1). In: Sih G.C. (eds) *Methods of analysis and solutions of crack problems*. Mech of fract 1:1-55 Springer, Dordrecht
71. Yau J, Wang S, Corten H (1980) A mixed-mode crack analysis of isotropic solids using conservation laws of elasticity. *ASME J Appl Mech* 47:335-341
72. Ansys Mechanical APDL Verification Manual (2021), VM267: Inclined cracked in 2-D plate under uniform tension loading. 757-758
73. Paris P, Erdogan F (1963) A critical analysis of crack propagation laws. *ASME J Basic Eng* 85:528-533
74. Erdogan F, Sih GC (1963) On the crack extension in plates under plane loading and transverse shear. *ASME J Basic Eng* 85:519-525
75. MSC software (2014) *MSC.Marc2014 User's manual*
76. <https://www.code-aster.org/spip.php?rubrique2> [accessed 21.11.21].
77. Geniaut S, eXtended finite element method: general information, *Code\_Aster Reference manual R7.02.12*, 2017.
78. Geniaut S, Massin P, Moës N (2005) Evaluation of stress intensity factors with G-theta method and level sets in *Code\_Aster*. 11th Int Conf of Fract, Turin, Italy